ARTICLE

Surface acoustic wave-driven pumpless flow for sperm rheotaxis analysis

Received 00th January 20xx,
Accepted 00th January 20xx

DOI: 10.1039/x0xx00000x

Junyang Gai[1], Citsabehsan Devendran[1], Adrian Neild[1,*], and Reza Nosrati[1,*]

Sperm rheotaxis, the phenomenon where sperm cells swim against the direction of fluid flow, is one of the major guiding mechanisms for long-distance sperm migration within the female reproductive tract. However, current approaches to study this pose challenges on dealing with rare sample by continuously introducing extra buffer. Here, we developed a device utilising acoustic streaming, the steady flow driven by an acoustic perturbation, to drive a tuneable, well-regulated continuous flow with velocities ranging from 40 µm s^{-1} to 128 µm s^{-1} (corresponding to maximum shar rates of 5.6 s^{-1} to 24.1 s^{-1}) in channels of interest - a range suitable for probing sperm rheotaxis behaviour. Using this device, we studied sperm rheotaxis in microchannels of distinct geometries representing the geometrical characteristics of the inner-surfaces of fallopian tubes, identified sperm dynamics with the presence of flow, and provided insights for understanding sperm navigation strategy in the female reproductive tract, where rheotaxis sperm swim near the boundaries to overcome the flow in the female reproductive tract and reach the fertilization site. This surface acoustic wave device presents a simple, pumpless alternative for studying microswimmers within in vitro models, enabling the discovery of new insights into microswimmers' migration strategies, while potentially offering opportunities for rheotaxis-based sperm selection and other flow-essential applications.

Introduction

Sperm migrate through the complex anatomical and physiological conditions of the female genital tract to reach the oocyte[1,2] . Three main natural mechanisms guide the sperm to navigate the female reproductive tract, namely thermotaxis (swimming along a temperature gradient)[3], chemotaxis (swimming towards a rising concentration of a chemoattractant)[4], and rheotaxis (swimming against the flow direction)[2]. Of these, rheotaxis is the main long-range mechanism that is present through most of the female reproductive tract to guide sperm. Rheotaxis is mostly investigated with the aid of microfluidic systems, enabling fluid handling and manipulation at biologically relevant scales (2 µm-1 mm) with precision, and acting as a suitable in vitro model for studying the behaviour of microswimmers. Microscopic inspection over the female fallopian tube shows a complex microenvironment composed of soft and highly folded epithelial tissue, forming confined longitudinally oriented microchannels with width ranging from around 20 µm to over 150 µm[2,5,6]. By realising micro-geometries which mimic the *in vivo* environment in the female reproductive tract, microfluidic systems have been developed to probe sperm hydrodynamic interactions, such as boundary following behaviour[7], sperm's inclination to cross laminar flow streamlines[8], as well as sperm's response to an external stimuli[9–11]. However, the complexity of pumping and tubing systems that has been used to drive these systems hindered clinical application/translation including decreasing the collected concentration of sample as pumping fluid will introduce more buffers, as well as increasing difficulties on retrieving sample from the microfluidic system.

Approaches, such as using fluid energy or external devices, to control fluid in an accurate and efficient manner in the microfluidic channel has been explored over the past decade[12]. In pump-based systems, an external syringe pump or pressure pump is used to drive the flow by creating a pressure gradient along the channel[13]. In addition , surface-tension driven microfluidics leverages the pressure difference between connected droplets of different radius to drive a fluid flow from one droplet towards the other one, with the flow velocities dictated by the volume of the droplet[14,15]. In the context of sperm rheotaxis, Zaferani et al.[11] and Sarbandi et al.[16] flushed sperm samples with a syringe pump through a microfluidic channel with physiologically relevant micro-geometries collecting the sperm which reorient and swim against the flow. Despite of the effectiveness of these methods in regulating the flow velocity, external accessories, such as tubing and connections are necessary to interface the microfluidic system with the fluid pump which increases the fluid dead volume. Cho

[a] *Department of Mechanical and Aerospace Engineering, Monash University, Clayton, Victoria 3800, Australia Address here. Emails: Reza.Nosrati@monash.edu (R.N.); Adrian.Neild@monash.edu (A.N.). Phone numbers: +61 3 990 53627; +61 3 990 54655.*

Electronic Supplementary Information (ESI) available: [details of any supplementary information available should be included here]. See DOI: 10.1039/x0xx00000x

et al.[8] and Rappa et al.[17] exploited the hydrostatic pressure difference, induced by the differential fluid volume between the inlet and outlet fluid chamber. However, this method is not capable of generating a steady velocity profile over a relatively long time span[15], limiting the observation period and reducing the effectiveness of this technique. Moreover, both of these methods serve as continuous flow systems, associated with increasing sample volume while inevitably introducing large volumes of external fluid contained in the interfaces in the microfluidic system, in turn posing challenges when dealing with rare or low concentration samples.

In contrast, integrating microfluidic systems with external force fields generated by optical[18], magnetic[19], dielectrophoretic[20] or acoustic effects[21–25] can be exploited to manipulate objects within microfluidic systems. In comparison with other methods, acoustic based microfluidics is particularly suitable for bio-applications, as it offers a biocompatible approach[26], and is capable of generating controlled, steady flows[27]. When acoustic waves propagate through a fluid, body forces are created on the fluid and flow will ensue[28], these steady flows are known as acoustic streaming[29]. There are two primary acoustic actuation methods widely used in microfluidics, both use piezoelectric components as a transducer, the wave is either created through the bulk of that component (bulk acoustic wave or BAW), or is established such that it is confined to the surface (surface acoustic wave or SAW). Typically, SAW induces vorticial flow in the confined fluid when SAW impinges on the liquid and refracts into the fluid in the form of longitudinal wave[24]. To date, SAW induced acoustic streaming has been utilized for tasks such as fluid mixing and actuation[30–32], cell patterning and translation[33], as well as droplet manipulation and modulation[34].

In this study, we use SAW driven acoustic streaming as a mechanism to allow on-demand, rapid and accurate regulation of flow within a microfluidic system, and apply this to probing sperm rheotaxis. In contrast to conventional hydrodynamic methods, the velocity, timing, as well as flow pattern, can be controlled independent of external motors or fluid surface energy. Utilizing this in vitro model, we investigated sperm rheotaxis and the interactions between sperm boundary following and rheotaxis behaviour in a fluidic environment representative of the female reproductive tract. We validated the capability of the device to establish rheotaxis zones for sperm to reorient in the presence of a flow by comparing sperm swimming patterns with and without SAW actuation. Subsequently, we revealed the interactions between sperm boundary following and rheotaxis behaviour by measuring and analysing sperm motility parameters and swimming patterns in various microgeometries within the device, mimicking the crevice-like inner surfaces of fallopian tubes. This simple, pumpless flow generation approach provides a novel platform for studying sperm hydrodynamic behaviour in female reproductive tracts, demonstrates the potential to select sperm based on its rheotaxis characteristics while avoiding dilution through the continuous additional pumped buffer.

Methodology

Device fabrication

The device comprised of an array of 50 µm height microfluidic channels in polydimethylsiloxane (PDMS) bonded onto a SAW device with a 32 µm wavelength (133 MHz). The width of the microchannels in the device ranges from 50 µm to over 225 µm, mimicking the relevant range of microgeometries present in the female reproductive tract[1,35] . The SAW device included a set of interdigitated transducers (IDTs) with 31 finger pairs patterned on a 0.5 mm thick, double-side polished, 128° Y-cut, X-propagating lithium niobate substrate. The SAW device was fabricated by depositing 10 nm chromium (adhesive layer for promoting adhesion between the substrate and the main conductive layer), 200 nm gold (conductive layer), and an additional 5 nm chromium (adhesive layer for improving adhesion of the final silicone-dioxide layer) on the lithium niobate substrate using E-beam evaporation. A 400-nm layer of silicone-dioxide was used to promote bonding and insulation between the IDTs and the PDMS layer. To fabricate the microfluidic device in PDMS, a silicon wafer mould with the geometry of the microchannels made of SU8 was prepared, followed by silanisation, where a layer of silane was deposited on top of the wafer to facilitate removal of the PDMS channel[36]. 10g PDMS and 2g curing agent were mixed at 1:5 weight ratio (SYLGARD® 184, Dow Corning) and cast over the mould, then degassed and left on a 70℃ hotplate for at least 3 hours, forming a 2mm-depth PDMS layer on top of the mould. A 1.5 cm-diameter biopsy punch was used to cast the unwanted PDMS, forming the fluid reservoirs. The flow resistance in the microchannel is 10^{-5}-fold that of the fluid reservoir, effectively eliminating fluid mixing in the microchannel and the fluid reservoir. To avoid difficulties in visualisation caused by channel deformation induced by SAW actuation, a non-standard mixing ratio of 1:5 was used to increase the stiffness of the PDMS layer. The PDMS layer and the SAW device were bonded together aided by air plasma treatment.

Sample Preparation

Cryogenically preserved bull semen samples purchased from ABS Global were thawed in 37 °C water bath for one minute, then extracted from the straw using an artificial insemination syringe prior to experiments. The microfluidic channel was pre-filled with a HEPES buffer[37] consisting of (HEPES (4-(2-Hydroxyethyl)piperazine-1-ethanesulfonic acid) (21 mM), $MgSO_4$ (0.8 mM), $NaHCO_3$ (4 mM), $Na_2HPO_4{\cdot}2H2O$ (0.8 mM), Na pyruvate (0.33 mM), and Na lactate (21.4 mM), KCL (5.3 mM), NaCl (117 mM), $CaCl_2$ (2.3 mM), , phenol red (0.03 mM), and D-glucose (5.5 mM)) supplemented with PVA (poly(vinyl alcohol)) (1 mg/mL) to prevent cell adhesion.

Experimental Procedure

To overcome the high hydraulic resistance in the microchannel with multiple channel decorations, the device was submerged in buffer under vacuum pressure for at least two hours to effectively load the microchannel, note that this prefilling of the channels is the only addition of buffer required, there is no requirement to continuously pump in additional buffer to

generate the flow. The device was then incubated at 37 °C for at least 15 minutes to reach a physiologically relevant temperature. The device was then mounted on an inverted IX83 fluorescence microscope (Olympus, Japan) equipped with an ORCA-Flash4.0 V3 Digital CMOS camera (Hamamatsu Photonics, Japan), and 2 µL of bull sperm was then introduced at the inlet (fluid reservoir 1). The flow (due to sample addition) was allowed to stabilise in the device for a period of 10 minutes. Meanwhile motile sperm from raw semen sample introduced at the inlet fluid reservoir swimming out of the seminal fluid into the main microchannel filled with buffer. After observing motile sperm in the microchannel, a 20 s image sequence in bright-field was recorded with a 20x magnification lens (Olympus, UPLXAPO 20X) and at 27 frames per second, and 5-10 s into the image sequence, the SAW field was actuated to induce a controlled flow field from fluid reservoir 2 to fluid reservoir 1 in the device. The focal plane of the objective was adjusted to be located at 20 µm from the bottom surface of the microchannel, where the highest number of motile sperm was observed (the white dashed line in Fig. 1). To generate the SAW field, a sinusoidal signal of 133 MHz, consistent with the operating frequency of the SAW device, was applied across the IDTs using a signal generator (BelektroniG F20 Power Saw, Freital, Germany). The flow velocity in the device after SAW actuation was quantified by tracking microparticles (500 nm-diameter) in the field of view. To quantify sperm motility parameters, the swimming trajectory of sperm was manually tracked in ImageJ, and the tracking results were analysed using a custom-written MATLAB code to quantify curvilinear velocity (VCL - instantaneous velocity along the swimming trajectory), straight line velocity (VSL - the distance between the first and last tracked points divided by the total tracking time), and the amplitude of lateral head displacement (ALH - time-averaged deviation of sperm head from its time-averaged swimming path). All motility parameters reported are actual sperm swimming parameters (relative to the channel walls). The angles of sperm migration trajectories were calculated as the angle of the displacement vector between the first and last tracking points relative to the direction of the positive X axis.

Simulation

The channel geometry and the measured averaged flow velocity were used in a custom-written script in MATLAB to obtain three-dimensional (3D) flow velocity and shear rate profiles in the device (Fig1c-d, ESI Figure S1-5), where the solution for Poiseuille flow was used[38]:

$$\rho(V.\nabla)V = -\nabla P + \mu(\nabla^2 V)$$

$$\nabla.V = 0$$

Device Characterisation

A quiescent homogeneous solution of fluorescent 500 nm polystyrene microparticles (Magsphere, Pasadena, CA, USA), diluted with a HEPES buffer, which filled the microfluidic channel, was used for device characterisation. To study the flow velocities in the regions of interest in the microfluidic channel, particle movements were visualized via a fluorescence microscope (Olympus BX43) and captured by a PixeLink (PL-B782U usb2) CCD colour camera. The average flow velocity was calculated by tracking the movement of polystyrene beads within the flow using imageJ.

System Principle

To generate a regulated flow field for probing sperm dynamics, a pump-less, acoustic-driven microfluidic system was developed using the acoustic streaming effect. By applying an oscillating electrical signal across the IDTs (Fig. 1a), a travelling SAW (TSAW) was generated that propagates along the substrate towards the Fluid Reservoir 1 in the PDMS layer. When TSAW interacts with the fluid reservoir, the acoustic energy diffracts into the liquid, giving rise to first-order (harmonic) velocity fluctuations. Due to gradients of these velocity fluctuations within the fluid and the resulting time-averaged body force acting on the fluid present on SAW propagation path (Figure S11), the rest of the fluid will replenish for the actuated fluid that moves along TSAW propagation direction, thus a second order flow (steady) is formed, known as acoustic streaming[39,40]. As depicted in Fig. 1a, the fluid reservoir was strategically placed near the end of the IDTs, this increased the first order velocity gradients along the x axis, and ensured that the acoustic waves did not directly impinge on the sperm in the region of interest, hence radiation forces could not act on the sperm[41] and the ultrasound would not be affecting the sperm motility[42]. This acoustic streaming effect drives a continuous flow within the device from Fluid Reservoir 2 towards Fluid Reservoir 1 (ESI Movie 1) upon SAW actuation, where the average flow velocity in each part of the device can be controlled using the applied acoustic power (Fig. 1b), which ranged from 1.1 to 2.0 W at 133 MHz. As the acoustic streaming occurs in the fluid reservoir 1, this in turn drives a laminar flow within segmented microchannels separated by the channel decorations designed in the main channel, resembling a Poisueille flow (ESI Movie 5). Thus, for simplicity, a Poisueille flow model was used to represent the flow distribution in each microchannel at the regions of interest. Moreover, the increased hydraulic resistance in the segmented microchannels limits the flow rate to generate average flow velocities at the regions of interest within the range of 40 µm s^{-1} to 128 µm s^{-1} in the segmented microchannels of different width. (corresponding to maximum shear rates of 5.6 s^{-1} to 24.1 s^{-1} across the channel), ideal for sperm rheotaxis (Fig. 1b-d, ESI Figure S1-5). To represent different flow and geometrical conditions within the female fallopian tube[6], sperm rheotaxis were studied both in less confined areas away from the walls (Region of Interest 1 – ROI 1, Fig. 1a) and in relatively small (50 µm in width) and relatively large (225 µm in width) microchannels (Region of Interest 2 – ROI 2, Fig. 1a).

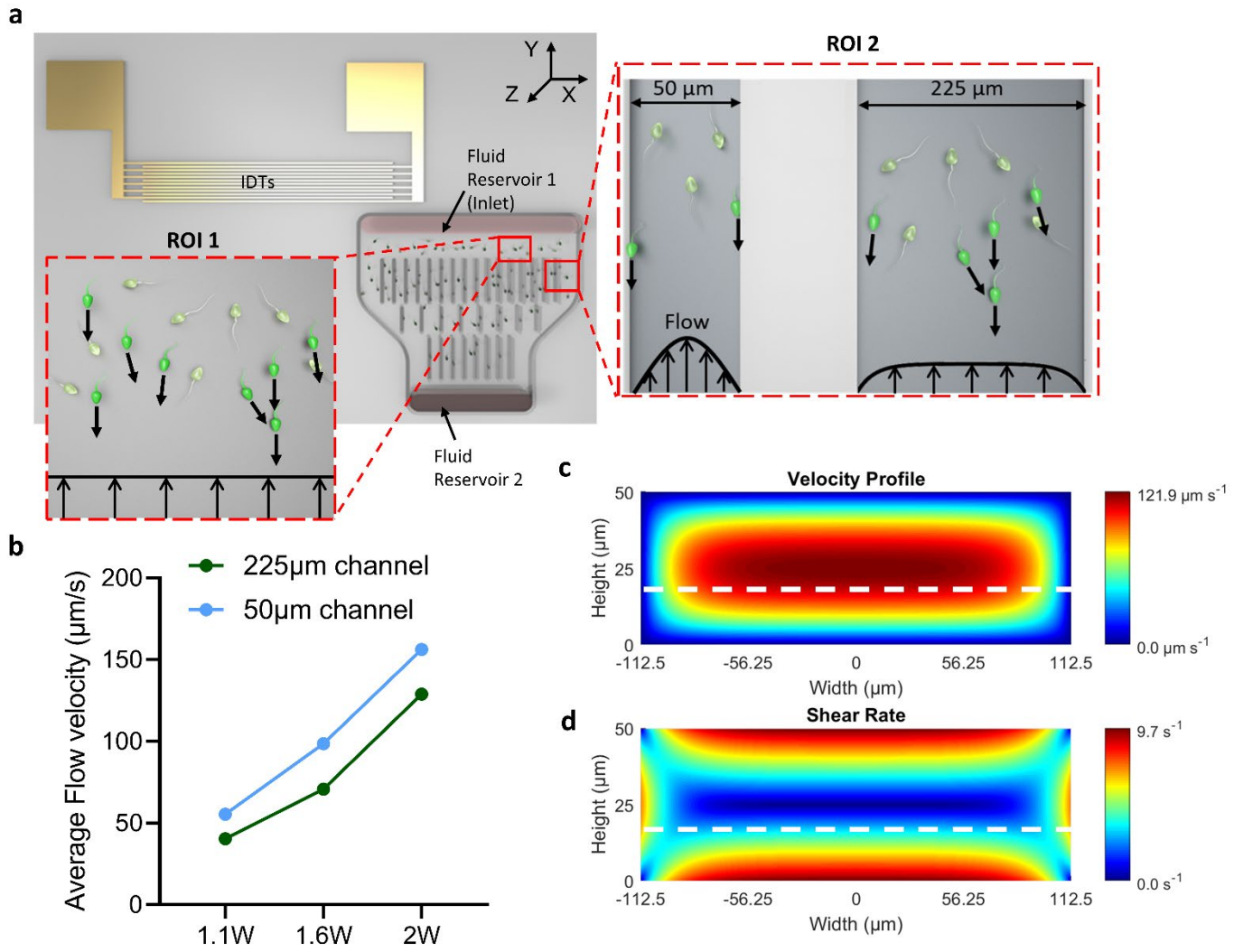

Figure 1. Acoustic-driven pumpless microfluidic device for sperm rheotaxis. (a) A representative schematic of the device indicating region of interest 1 (ROI 1) and region of interest 2 (ROI 2) where sperm rheotaxis in the bulk fluid and in microchannels were studied, respectively. By inducing a flow using acoustic streaming effect, motile sperm (green) exhibited a rheotactic behaviour to reorient and swim against the flow, while poorly motile sperm (yellow) were swept downstream by the flow. (b) The average flow velocity in the microchannels as a function of applied acoustic power (generator power level) at 133 MHz. Representative (c) flow velocity and (d) shear rate profiles in the cross-sectional area of 225 µm microchannels at the average velocity of 70µm s^{-1}. The imaging plane (focal plane of the objective) was located at 20 µm from the bottom surface of the microchannel, as indicated by the white dashed line.

Results and Discussion

The pump-less acoustic-driven system was used to generate stable flow conditions in the device and study sperm rheotaxis. Sperm swimming trajectories were imaged in ROI 1, in the bulk fluid and away from the microchannel walls, with and without inducing an acoustic-driven flow field. In the absence of flow, sperm swim randomly in all directions (Fig. 2a, ESI Movie 2), with their swimming trajectories randomly oriented in all directions with respect to X-axis (Fig. 2c,e). However, upon actuating the IDTs at 1.6 W, a steady flow field with an average flow velocity of 40 µm s^{-1} (corresponding to a shear rate of 4.8 s^{-1}) was generated in ROI 1 to enable sperm rheotaxis. Sufficiently motile sperm reoriented, confined their swimming trajectories within 103° to 245° and exhibited rheotaxis to swim against the flow while non-motile sperm and debris were advected downstream by the flow (Fig. 2b,d, and ESI Movie 2, n=65). The swimming trajectories of sperm that exhibited rheotaxis shifted significantly in comparison with the orientation of randomly swimming sperm in the absence of flow (Fig. 2a,c, n=65). These observations are consistent with previous literature [2,43,44], where in the presence of flow, the interaction between sperm flagellar envelope and the flow re-orients the cell to align its body in the opposite direction of the flow[11] – a long-range navigation strategy for sperm to swim through the female reproductive tract. It is noteworthy that shear flow acts as one of the sperm selection mechanisms *in vivo*, as this behaviour is dependent on sperm motility level. This experiment confirmed the capability of our simple platform to provide a relevant range of flow velocities and shear rates on-demand for sperm rheotaxis, without utilizing any external pumping systems

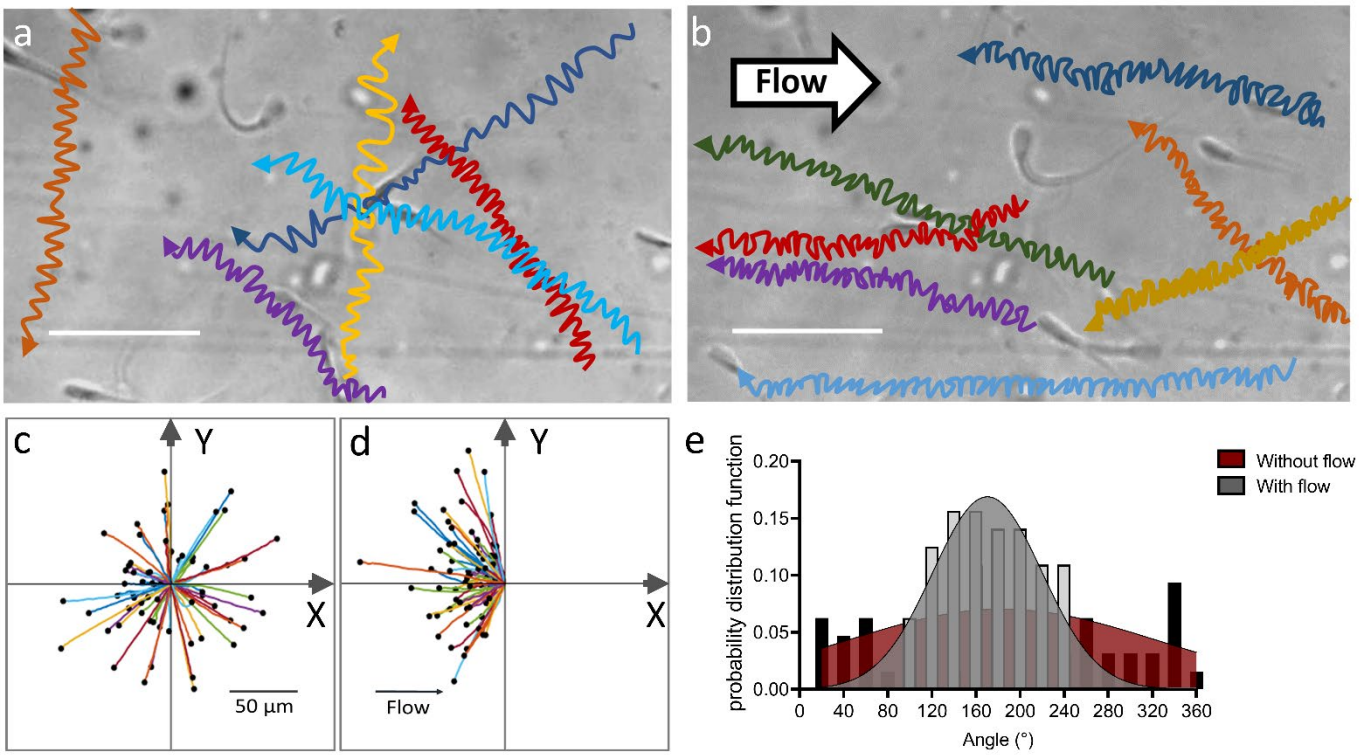

Figure 2. Sperm swimming behaviour in the bulk fluid in ROI 1 (a) without and (b) with inducing an acoustic-driven flow field at 1.6 W. The swimming trajectories of sperm (c) in the absence and (d) in the presence of an acoustic-driven flow field in ROI 1 (see ESI Movie 2), and (e) the histogram of their corresponding orientation angles with respect to X-axis. All swimming trajectories were overlaid to start at (0,0) and end at the black dot from five independent experiments using identical SAW chip with two different microchannels. >10 sperm were analysed each experiment (65 trajectories analysed in total). *p*-values were determined by an unpaired t test with Welch's corrections, $p \leqslant 0.01$. Scale bars in a and b: 50 µm.

To study dynamics of sperm transport in longitudinal microchannels of various width present in female reproductive tract[45,46], our system was designed to consist of 50-µm-wide and 225-µm-wide microchannels and the applied acoustic power was regulated (at 133 MHz frequency and 1.1 to 2.0 W generator power level) to generate flow velocities ranging from 40 µm s^{-1} to 128 µm s^{-1} (corresponding to maximum shar rates of 5.6 s^{-1} to 24.1 s^{-1}) in the microchannels.

In the 50-µm-wide channel (Fig. 3) and in the absence of flow, the majority of sperm exhibited the boundary-following behaviour to swim along the channel walls due to hydrodynamic interactions with the surface. Upon actuating the IDTs at 1.1 W, a flow field with an average velocity of 55 µm s^{-1} (corresponding to a shear rate of 10 s^{-1}) was generated in the microchannel (see ESI Figure S3). Despite motile sperm exhibit rheotaxis behaviour by showing swimming direction being against the flow, not all of them were able to make progressive movement in a flow environment. As shown in Fig. 3 and ESI Movie 3, by inducing a flow in the microchannel, some motile sperm were swept downstream due to the induced drag, these cells termed as insufficiently motile sperm, whilst some motile sperm were able to actively swim against the flow and continue to follow the channel walls, termed as sufficiently motile sperm. Fig. 3a-b show representative trajectories of insufficiently motile and sufficiently motile sperm, where the swimming trajectory of sufficiently motile sperm was confined within ~8 µm of the surface. In comparison, insufficiently motile sperm exhibited a larger lateral displacement with their swimming trajectories confined within ~20 µm of the surface.

Fig. 3c compares the curvilinear velocity (VCL) of insufficiently motile and sufficiently motile sperm in the 50-µm-wide microchannel prior to exposure to the flow field. Sufficiently motile sperm showed an average VCL of 101 ± 25 µm s^{-1} (n = 65) without any competitive advantage over insufficiently motile

sperm (with VCL of 100 ± 21 µm s^{-1}, not statistically significant, n=65) with respect to their swimming speed. This suggests that the instantaneous swimming velocity of sperm along its trajectory may not be the determining factor for rheotaxis sperm to overcome the flow. In contrast, Fig. 3d shows the lateral head displacement (ALH) of sufficiently motile sperm in comparison with insufficiently motile sperm, where insufficiently motile sperm demonstrated a significantly higher ALH of 9 µm, 23 % higher than the ALH for sufficiently motile sperm (~7.3 µm), indicating the importance of lateral head displacement in the capability of rheotaxis sperm being progressive motile in a flow environment. These results suggest that within relatively narrow regions of the female fallopian tube, rheotaxis sperm that beat with smaller flagellar amplitudes and subsequently swim with smaller lateral displacements gain a potential advantage over other population of rheotaxis sperm to overcome the incoming flow and reach the site of fertilization.

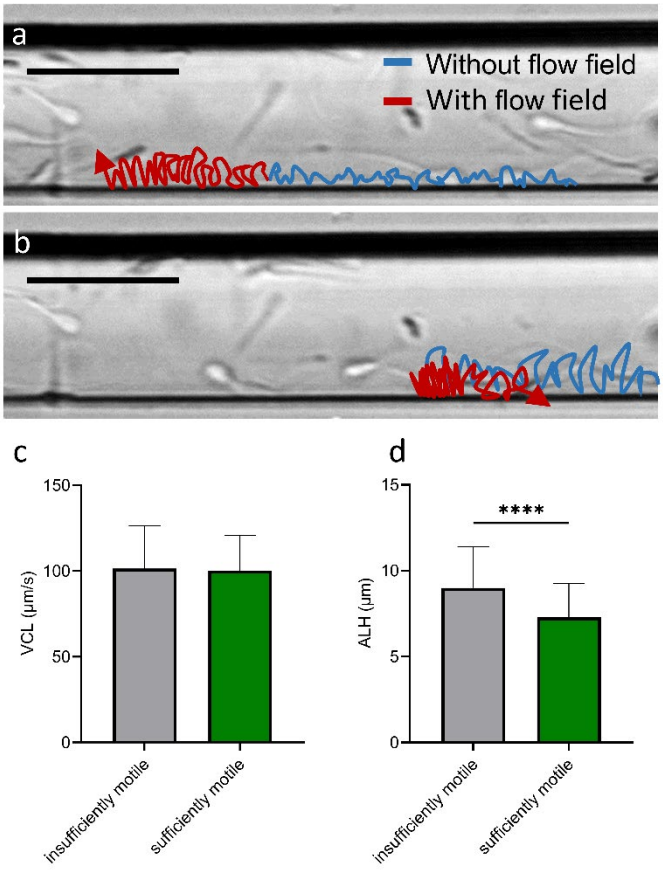

Figure 3. Motility analysis of sufficiently motile sperm and insufficiently motile sperm in a 50-µm-wide channel. Representative sperm swimming trajectories of (a) sufficiently motile sperm and (b) insufficiently motile sperm (see ESI Movie 3) in the absence (blue trajectories) and in the presence (red trajectories) of flow. A comparison of (c) curvilinear velocity (VCL) and (d) lateral head displacement (ALH) for insufficiently motile sperm and sufficiently motile sperm swimming pattern prior to exposure to the flow field. *p*-values were determined by an unpaired t test with Welch's corrections, ****$p \leqslant 0.0001$. Scale bars: 50 µm. All data represented as mean ± s.d.

The pumpless acoustofluidic approach was also used to study the migration directions of rheotaxis sperm in 225-µm-wide microchannels (Fig. 4), representing relatively large microgrooves *in vivo*. In a 225-µm-wide channel, the migration directions of rheotaxis sperm that could overcome the flow and swim upstream was flow (shear rate) dependent. At higher flow velocities, rheotaxis sperm was observed to migrate across the flow streamlines (across the width of the microchannel) towards the other side of the channel as opposed to swimming directly against the flow (Fig. 4a-f). At the relatively low flow velocity of 40 µm s^{-1} (corresponding to a shear rate of 4.0 s^{-1}), the majority of sperm that overcome the flow swim directly against the flow, confining their swimming trajectories within 131° to 222° of the positive x axis with their probability distribution function (PDF) indicating a sharp peak at 168° (Fig. 4a,d,g, see ESI Movie 4, n = 55). As the flow velocity increased to 70 µm s^{-1} (corresponding to a shear rate of 7.1 s^{-1}), a subpopulation of sperm oriented tilted with respect to the flow direction and migrated across the flow streamlines, as opposed to swimming directly against the flow (Fig. 4b,e, see ESI Movie 4, n = 55), with their trajectory oriented more widely with respect to positive x-axis at 96° to 247° (Fig. 4g). The PDF also indicated a bimodal distribution with a fit to our data indicating two peaks at around 128° and 191° (Fig. 4g). This behaviour to swim across the flow streamlines was further amplified at the flow velocity
of 130 µm s^{-1} (corresponding to a shear rate of 9.9 s^{-1}), providing the widest coverage of the angles, ranging from 97° to 267° (Fig. 4c,f,g, see ESI Movie 4, n = 55), and the PDF showed two peaks at 132° and 244°. Trajectory analysis shows that approximately half of the cells oriented tiled with respect to flow directions respond to the flow by making a right turn while the other half turned left. This bimodal distribution originates from the inherent morphological characteristics of each individual sperm to either turn left or right in response to the applied velocity field[47]. Sperm turning direction is potentially dependent on the level of midpiece asymmetry, causing the head of a right-turning sperm with an asymmetrical midpiece to act as a tilted hydrofoil while sperm with a symmetrical midpiece turn left as a consequence of the inherent rolling direction of their flagellar envelope[47]. In addition to sperm morphology, the average angle between the longitudinal axis of sperm head and the flow direction (see ESI Figure S8) also contributed to this hydrofoil effect. When sperm body was fully aligned with the flow direction, sperm tend to swim directly against the flow (ESI Figure S6, S8a), but swim across the flow streamlines to reach the other side of the channel when the head was oriented tilted with respect to the flow direction (ESI Figure S7, S8b, c, see ESI Movie 4). Furthermore, the flow drag component that alternates sperm migration directions is a function of flow velocity and sperm orientation angle. Drag increases with the increase of sperm orientation angle and flow velocity, resulting from the alignment of longitudinal axis of sperm body with the flow. Our result suggests a decrease in rheotaxis sperm that oriented parallel to the flow percentage with an increase in flow velocity, indicating that sperm would swim in a more tilted manner (ESI Figure S9) with an increase in flow velocity in

female reproductive tract, as a result of this increased flow drag component.

Fig. 4h-j compares the motility parameters for rheotaxis sperm in a 225-µm-wide microchannels as a function of flow velocity. The VCL and VSL significantly increased by increasing the flow velocity, indicating the swimming behaviour of rheotaxis sperm at higher flow velocities to swim straighter and faster. Specifically, VCL increased by 24% and 48% by increasing the average flow velocity from 40 µm s^{-1} to 70 µm s^{-1} and 130 µm s^{-1}, respectively ($p \leq 0.001$ in both cases). VSL also indicated a similar trend, increasing from 25 µm s^{-1} at 40 µm s^{-1} to 32 µm s^{-1} (by 28%) and 51 µm s^{-1} (by 59%) at 70 µm s^{-1} and 130 µm s^{-1}, respectively ($p \leq 0.01$). Moreover, the percentage of sperm exhibiting rheotaxis behaviour reduced by 33% and 44% by increasing the average flow velocity from 40 µm s^{-1} to 70 µm s^{-1} and 130 µm s^{-1}, respectively (Fig. 4j). This reduction in the percentage of sperm that can swim upstream in the flow environment, and increase in the average sperm velocity that overcome the flow at higher flow velocities, are attributed to the reduced number of sufficiently motile sperm in the sample that can overcome the induced drag at higher flow velocities, only allowing highly motile sperm to overcome the flow in the presence of a higher flow velocity and shear rate. This result has provided new insight for understanding sperm navigation strategy in a relatively wider region in female reproductive tract, where sperm tend to move across the flow streamlines to reach the other side of the channel, providing sufficient flow drag force when sperm are oriented tilted with respect to the flow direction. Furthermore, rheotaxis sperm exhibit a significantly higher VCL and VSL with the increase of flow velocity, suggesting an opportunity for tuneable rheotaxis-based sperm selection without introducing external fluid to dilute the concentration using this device.

ARTICLE

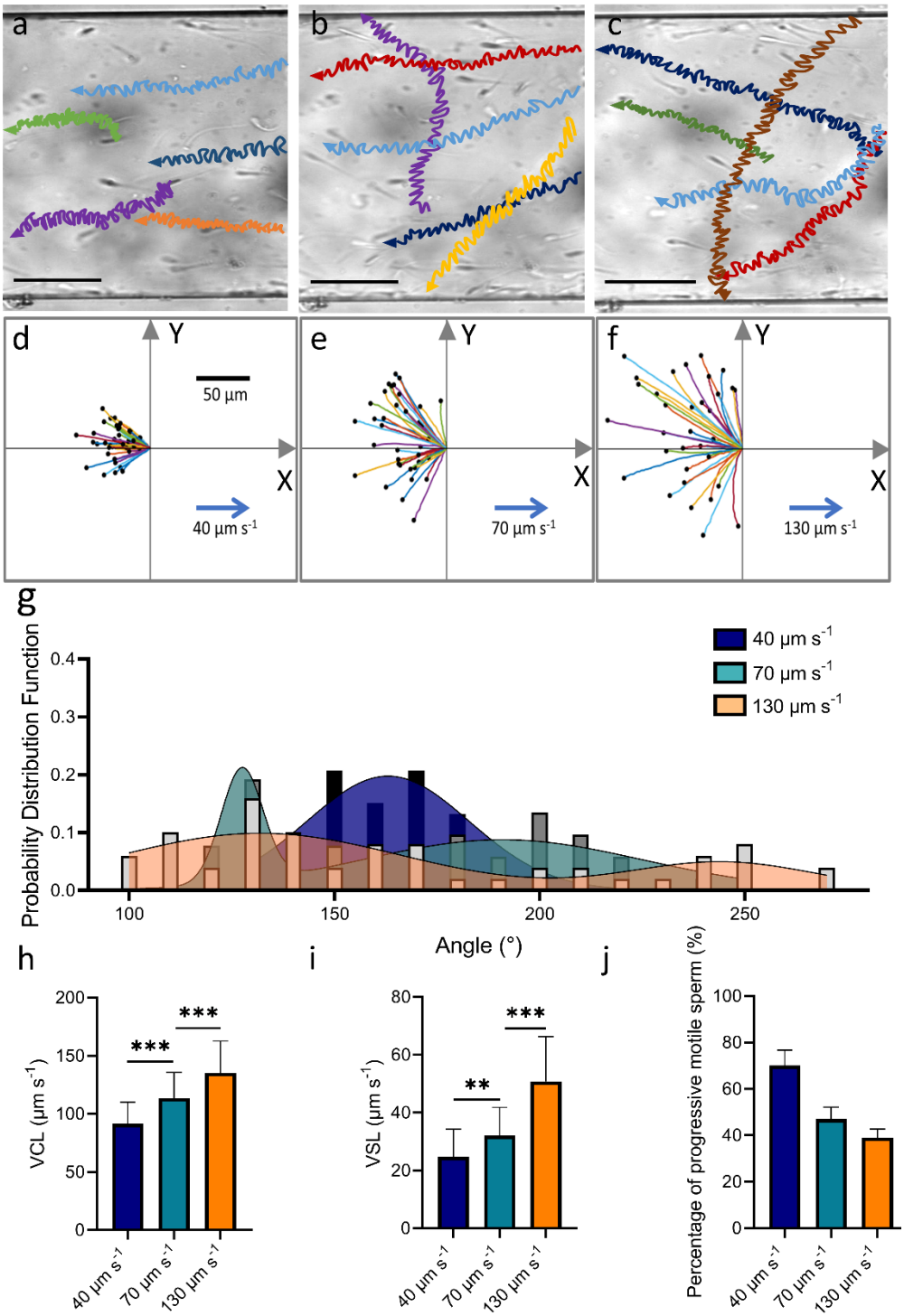
a
b
c
d
e
f
Y
X
50 µm
40 µm s-1
70 µm s-1
130 µm s-1
g
Probability Distribution Function
0.0
0.1
0.2
0.3
0.4
100
150
200
250
Angle (°)
40 µm s-1
70 µm s-1
130 µm s-1
h
i
j
VCL (µm s-1)
VSL (µm s-1)
Percentage of progressive motile sperm (%)
***
**
40 µm s-1
70 µm s-1
130 µm s-1

Figure 4. Sperm rheotaxis behaviour in 225-µm-wide microchannels. Representative trajectories of rheotaxis sperm in a flow field with an average velocity of (a) 40 µm s^{-1} (see ESI Movie 4), (b) 70 µm s^{-1} (see ESI Movie 4) and (c) 130 µm s^{-1} (see ESI Movie 4) with the corresponding overlaid trajectories shown in (d), (e) and (f), respectively (corresponding to an applied acoustic power at generator power level of 1.1 W, 1.6 W and 2 W, respectively). Each trajectory is 1.8 s. (g) The full histogram and probability distribution function (PDF) of the sperm orientation with respect to positive x axis as a function of flow velocity. A comparison of (h) curvilinear velocity (VCL), (i) straight line velocity (VSL) and (j) percentage of rheotactic sperm as a function of the average flow velocity. *p*-values were determined by one-way ANOVA test with Bonferroni corrections, $^{**}p \leqslant 0.01$ and $^{***}p \leqslant 0.001$. Scale bars: 50 µm. All data represented as mean ± s.d.

Conclusions

We present a novel acoustofluidic platform leveraging acoustic streaming and a microfluidic channel, allowing for on-demand, rapid and accurate regulation of flow without external pumps for sperm rheotaxis probing. The strategic placement of the IDTs in the device generates a tuneable and stable flow field, capable of inducing sperm rheotaxis by simulating the physiological conditions *in vivo*. In the context of sperm rheotaxis, our findings suggest a geometry-based sperm migration strategy against the flow in female reproductive tract. We identified the determining role of ALH in boundary-following, rheotaxis sperm migrating against the flow in a 50 µm channel, where non-sufficiently motile sperm demonstrated a 28 % higher ALH than sufficiently motile sperm. We also demonstrated two types of rheotaxis sperm in a 225 µm channel, sperm which swim parallel to the flow and sperm which migrate towards the channel boundaries in high-velocity fields. The percentage of rheotaxis sperm that migrate towards the channel boundaries increases with the flow velocity as a result of the proposed hydrofoil effect. Furthermore, the VCL of rheotaxis sperm increased by up to 52% by increasing the average flow velocity from 40 µm s^{-1} to 130 µm s^{-1}. In the context of biomedical applications, this acoustofluidic platform is reliable for driving fluid flow in a controllable and tuneable manner independent of external motor or fluid surface energy, providing an opportunity for rare sample handling without introducing extra buffer to dilute the concentration. In conclusion, this simple, pump-free approach to generate a regulated flow within a microfluidic channel has provided new insight for designing in vitro models for motility analysis of the microswimmers, and could potentially be applied to rheotaxis-based sperm selection as well as other flow-essential applications such as on-chip sample preparation platform[30] and sensors[48].

Conflicts of interest

There are no conflicts to declare.

Acknowledgements

This work was supported by the Australian Research Council (ARC) Discovery Project Grant (DP190100343 to R.N. and DP210103361 to A.N and R.N.). This work was performed in part at the Melbourne Centre for Nanofabrication (MCN) in the Victorian Node of the Australian National Fabrication Facility (ANFF).

References

1 R. Nosrati, P. J. Graham, B. Zhang, J. Riordon, A. Lagunov, T. G. Hannam, C. Escobedo, K. Jarvi and D. Sinton, *Nat. Rev. Urol.*, 2017, **14**, 707–730.
2 K. Miki and D. E. Clapham, *Curr. Biol.*, 2013, **23**, 443–452.
3 A. Bahat and M. Eisenbach, *Mol. Cell. Endocrinol.*, 2006, **252**, 115–119.
4 M. Eisenbach, *Dev. Genet.*, 1999, **25**, 87–94.
5 T. Fujii, *Microelectron. Eng.*, 2002, **61**–**62**, 907–914.
6 K. June Mullins and R. G. Saacke, *Anat. Rec.*, 1989, **225**, 106–117.
7 R. Nosrati, M. Vollmer, L. Eamer, M. C. San Gabriel, K. Zeidan, A. Zini and D. Sinton, *Lab Chip*, 2014, **14**, 1142–1150.
8 B. S. Cho, T. G. Schuster, X. Zhu, D. Chang, G. D. Smith and S. Takayama, *Anal. Chem.*, 2003, **75**, 1671–1675.
9 L. Xie, R. Ma, C. Han, K. Su, Q. Zhang, T. Qiu, L. Wang, G. Huang, J. Qiao, J. Wang and J. Cheng, *Clin. Chem.*, 2010, **56**, 1270–1278.
10 Y. Yan, B. Zhang, Q. Fu, J. Wu and R. Liu, , DOI:10.1039/d0lc00845a.
11 M. Zaferani, S. H. Cheong and A. Abbaspourrad, *Proc. Natl. Acad. Sci. U. S. A.*, 2018, **115**, 8272–8277.
12 P. K. Yuen, *Lab Chip*, 2013, **13**, 1737–1742.
13 L. Eamer, M. Vollmer, R. Nosrati, M. C. San Gabriel, K. Zeidan, A. Zini and D. Sinton, *Lab Chip*, 2016, **16**, 2418–2422.
14 G. M. Walker and D. J. Beebe, *Lab Chip*, 2002, **2**, 131–134.
15 T. E. De Groot, K. S. Veserat, E. Berthier, D. J. Beebe and A. B. Theberge, *Lab Chip*, 2016, **16**, 334–344.
16 I. R. Sarbandi, A. Lesani, M. Moghimi Zand and R. Nosrati, *Sci. Rep.*, 2021, **11**, 1–8.
17 K. Rappa, J. Samargia, M. Sher, J. S. Pino, H. F. Rodriguez and W. Asghar, *Microfluid. Nanofluidics*, 2018, **22**, 1–11.
18 B. Landenberger, H. Höfemann, S. Wadle and A. Rohrbach, *Lab Chip*, 2012, **12**, 3177–3183.
19 N. Xia, T. P. Hunt, B. T. Mayers, E. Alsberg, G. M. Whitesides, R. M. Westervelt and D. E. Ingber, *Biomed. Microdevices*, 2006, **8**, 299–308.
20 P. R. C. Gascoyne and J. Vykoukal, *Electrophoresis*, 2002, **23**, 1973–1983.
21 A. Haake, A. Neild, D. H. Kim, J. E. Ihm, Y. Sun, J. Dual and B. K. Ju, *Ultrasound Med. Biol.*, 2005, **31**, 857–864.
22 Y. Gu, C. Chen, Z. Mao, H. Bachman, R. Becker, J. Rufo, Z. Wang, P. Zhang, J. Mai, S. Yang, J. Zhang, S. Zhao, Y. Ouyang, D. T. W. Wong, Y. Sadovsky and T. J. Huang, *Sci. Adv.*, 2021, **7**, 1–11.
23 A. Lenshof, C. Magnusson and T. Laurell, *Lab Chip*, 2012, **12**, 1210–1223.

24 M. Gedge and M. Hill, *Lab Chip*, 2012, **12**, 2998–3007.
25 J. Gai, R. Nosrati and A. Neild, *Lab Chip*, 2020, 4262–4272.
26 J. Gai, E. Dervisevic, C. Devendran, V. J. Cadarso, M. K. O'Bryan, R. Nosrati and A. Neild, *Adv. Sci.*, 2022, **9**, 2104362.
27 G. Greco, M. Agostini, I. Tonazzini, D. Sallemi, S. Barone and M. Cecchini, *Anal. Chem.*, 2018, **90**, 7450–7457.
28 T. Cambonie, B. Moudjed, V. Botton, D. Henry and H. Ben Hadid, *Phys. Rev. Fluids*, 2017, **2**, 1–21.
29 X. Ding, P. Li, S. C. S. Lin, Z. S. Stratton, N. Nama, F. Guo, D. Slotcavage, X. Mao, J. Shi, F. Costanzo and T. J. Huang, *Lab Chip*, 2013, **13**, 3626–3649.
30 Y. Zhang, C. Devendran, C. Lupton, A. De Marco and A. Neild, *Lab Chip*, 2019, **19**, 262–271.
31 N. Zhang, A. Horesh and J. Friend, *Adv. Sci.*, 2021, **2100408**, 1–10.
32 L. Meng, X. Liu, Y. Wang, W. Zhang, W. Zhou, F. Cai, F. Li, J. Wu, L. Xu, L. Niu and H. Zheng, *Adv. Sci.*, , DOI:10.1002/advs.201900557.
33 D. J. Collins, B. L. Khoo, Z. Ma, A. Winkler, R. Weser, H. Schmidt, J. Han and Y. Ai, *Lab Chip*, 2017, **17**, 1769–1777.
34 H. Van Phan, T. Alan and A. Neild, *Anal. Chem.*, 2016, **88**, 5696–5703.
35 S. S. Suarez, *Cell Tissue Res*, 2016, **363**, 185–194.
36 B. G. Abdallah and A. Ros, *Surface coatings for microfluidic-based biomedical devices*, Woodhead Publishing Limited, 2013.
37 L. Eamer, R. Nosrati, M. Vollmer, A. Zini and D. Sinton, *Biomicrofluidics*, 2015, **9**, 044113.
38 H. Bruus, *Choice Rev. Online*, 2008, **45**, 45-5602-45–5602.
39 W. L. Nyborg, *J. Acoust. Soc. Am.*, 1958, **30**, 329–339.
40 T. Frommelt, D. Gogel, M. Kostur, P. Talkner, P. Hänggi and A. Wixforth, *IEEE Trans. Ultrason. Ferroelectr. Freq. Control*, 2008, **55**, 2298–2305.
41 J. Gai, R. Nosrati and A. Neild, *Lab Chip*, 2020, **20**, 4262–4272.
42 J. Gai, E. Dervisevic, C. Devendran, V. J. Cadarso, M. K. O'Bryan, R. Nosrati and A. Neild, *Adv. Sci.*, 2022, **2104362**, 2104362.
43 M. Zaferani, F. Javi, A. Mokhtare, P. Li and A. Abbaspourrad, *Elife*, 2021, **10**, 1–34.
44 M. Zaferani, G. D. Palermo and A. Abbaspourrad, *Sci. Adv.*, , DOI:10.1126/sciadv.aav2111.
45 C. K. Tung, L. Hu, A. G. Fiore, F. Ardon, D. G. Hickman, R. O. Gilbert, S. S. Suarez and M. Wu, *Proc. Natl. Acad. Sci. U. S. A.*, 2015, **112**, 5431–5436.
46 N. A. KALKHORAN, Sara; BENOWITZ, Neal L .; RIGOTTI, *Rev. del Col. Am. Cardiol.*, 2018, **72**, 2964–2979.
47 A. Bukatin, I. Kukhtevich, N. Stoop, J. Dunkel and V. Kantsler, *Proc. Natl. Acad. Sci. U. S. A.*, 2015, **112**, 15904–15909.
48 E. Dervisevic, N. H. Voelcker, G. Risbridger, K. L. Tuck and V. J. Cadarso, *Anal. Chem.*, 2022, **94**, 1726–1732.